Journal of
Synchrotron Radiation

ISSN 0909-0495

Received 25 June 2012
Accepted 4 October 2012

Ascertaining the nanocluster formation within an ion-irradiated Pt/Ni/C multi-trilayer with X-ray absorption spectroscopy

Nitya Ramanan,[a] Sumalay Roy,[b] Debdutta Lahiri,[a]* Surinder M. Sharma[a] and B. N. Dev[b]

[a]High Pressure and Synchrotron Radiation Physics Division, Bhabha Atomic Research Centre, Mumbai 400085, India, and [b]Department of Materials Science, Indian Association for the Cultivation of Science, Jadavpur, Kolkata 700032, India. E-mail: debduttalahiri@yahoo.com

In this work nanoclusters formed in a Pt/Ni/C multi-trilayer by the ion-irradiated method of synthesis are characterized. In particular, an attempt to understand the role of interfaces in the synthesis is made. With this objective, ion-irradiation-induced structural changes in a Pt/Ni/C multi-trilayer using X-ray absorption spectroscopy (at the Ni *K*-edge) in conjunction with the X-ray standing-wave technique are investigated. The XANES analysis identifies chemical binding at pristine Ni/C and Ni/Pt interfaces, in contrast with physical adsorption at the Pt/C interface. The chemical nature of the interfaces determines their relative stability with respect to irradiation and controls the extent of metallic diffusion. The most interesting structural change, upon irradiation, is the disruption of the Pt/C interface and subsequent migration of Pt atoms towards pre-diffused Ni atoms within the C layer, leading to the formation of Ni-centered Ni–Pt bimetallic nanoclusters (with Ni:Pt = 60:40). These clusters are highly disordered beyond their nearest neighbor and find wide-scale applications as, for example, magnetic devices *etc.* The implications of these findings on the design goals are discussed.

Keywords: XAFS; X-ray standing wave; multilayers; ion-irradiation; nanoclusters; synthesis.

1. Introduction

Synthetic multilayers (MLs) (Chakraborty, 1991) are widely investigated for their unique structural (McWhan, 1985), magnetic (Stearns, 1984) and electronic (Falco & Schuller, 1985) properties. They have a wide range of applications in X-ray optics (*e.g.* monochromators, mirrors), magneto-electronics (*e.g.* exchange bias) *etc*. The realisation of application potential of these synthetic MLs largely depends upon their microstructures (the interfaces in particular) (Sella *et al.*, 1998; Qin *et al.*, 2007). While the microstructure is often deliberately modified to tailor material properties [for example, inducing spin-reorientation transition (Weller *et al.*, 2000), magnetic–non-magnetic transition (Dev *et al.*, 2006) and, *vice versa*, introducing impurities (Bera *et al.*, 2007*b*), extending the energy range for reflectivity], it may become naturally modified/damaged during actual applications [*e.g.* heating (Nakajima *et al.*, 1992; Kapta *et al.*, 2004), X-ray beam impingement (Bera *et al.*, 2003; Takacs *et al.*, 1985)]. It is important to understand these structural changes in order to assess the stability of device functionality. In this work we report ion-irradiation-induced structural changes (Ghose, Goswami *et al.*, 2001; Bera *et al.*, 2007*b*; Wang *et al.*, 1994; Toulemonde *et al.*, 1992) (mixing behavior in particular) in a Pt/Ni/C depth-graded ML, using selective-fluorescence-mode extended X-ray absorption fine structure (EXAFS) measurements at the Ni *K*-edge. A Pt/C ML has been used as a regular X-ray mirror (Dev, 2003; Yamashita *et al.*, 1998). Addition of a Ni layer is expected to extend the functional energy range beyond 80 keV, *i.e.* beyond the Pt *K*-edge. Ion irradiation (Au^{2+}, 2 MeV) of the mirror at a fluence of 2×10^{15} ions cm^{-2} is intended to simulate the defects that could possibly be induced by high-flux high-energy X-rays.

However, the real impact of this work lies beyond mirror assessment in terms of damage. Instead, we investigate the feasibility/possibility of utilizing the irreversible structural changes to synthesize bimetallic clusters on a C matrix. Some of the important applications of bimetallic clusters in this configuration include: (i) spintronics, Ni/Pt magnetic clusters on a non-magnetic C matrix for patterned ultrahigh-density magnetic recording media (Bera *et al.*, 2006); (ii) nano-barcodes, offering mass-memory capacity for identifying probes in biomolecules (Nicewarner-Peña *et al.*, 2001; Zhang *et al.*, 2009); (iii) conductive ink (on substrates), for the

fabrication of electronic circuit elements. A bimetallic solution eliminates the requirement of a molecular weight stabilizer for monometallic nanoparticles (Chopra *et al.*, 2009) and the related pre-heating issues; (iv) fuel cells (Prabhuram *et al.*, 2004), while Pt has been the traditional electro-catalyst in fuel cells, it is prone to CO poisoning; alloying with Ni controls this poisoning (Deivaraj *et al.*, 2003); (v) catalysts: (*a*) for hydrogenation of olefins and structural rearrangement (of the carbon skeleton) in hydrocarbons (Toshima & Yonezawa, 1998), (*b*) for decontamination of ground water (Wong *et al.*, 2008), (*c*) metal-filled carbon nanotubes as electrocatalysts in fuel cells (Che *et al.*, 1999); (vi) nanomotors, to mimic biomotors present in biological systems (Wheat *et al.*, 2010); bimetallic nanoparticles are necessary for automated motion of these motors; (vii) lubricants, for MEMS switch contacts (Patton *et al.*, 2008). Bimetallic nanoparticles offer the advantage of durability at high current and reduced adhesion compared with monometallic nanoparticles.

With wetting being an issue in electronic devices, the ion-irradiation method would provide an advantage over precursor-dependent chemical routes of wet synthesis, *e.g.* the sol–gel method (Jiang *et al.*, 2004), colloidal synthesis (Nose *et al.*, 2009). Further, the control parameter for composition of the bimetallic clusters will not be limited to thermodynamics alone, but can be controlled by collision kinetics and the initial thickness of the layers as well.

In this context, our structural probe would provide a first-hand impression (Roy *et al.*, 2012; Bera *et al.*, 2007*b*) of the cluster structure for the given irradiation condition. For example, our results would establish whether Ni and Pt form isolated clusters in the C-matrix or core-shell structure (Wang *et al.*, 2010; Li & Haldar, 2010) or alloy. These predictions cannot be drawn simplistically from bulk binary phase diagrams since factors such as surface energetics (Lahiri *et al.*, 2005), Ni/C or Pt/C interactions (*i.e.* ternary phase diagrams), could come into play.

Broader techniques such as X-ray reflectivity (Ghose & Dev, 2001) on the pristine ML have provided information on layer periodicity and roughness. Cross-sectional transmission electron microscopy (XTEM) (Roy *et al.*, 2012) and fluorescence studies (by our group), on the irradiated ML, revealed mixing of Ni–Pt layers and modified C layers containing nanoclusters. From the XTEM micrographs the average diameter of the clusters was determined to be $\sim$1.7 nm, with a size dispersion of $\sim$10%. The average inter-cluster separation was determined to be $\sim$3.6 (0.9) nm and 0.8 (0.1) nm across the plane of the C layer. However, these techniques are unable to ascertain the atomic origin or nature of these ion-irradiation-induced clusters. For example, questions like (i) whether the inter-layer mixing is physical or chemical; (ii) why one interface is more susceptible compared with the others; (iii) whether the Ni/Pt atoms in the C layer exist as isolated clusters or form nano-alloys; (iv) approximate composition and degree of order of these clusters, remain unanswered. We attempt to address these questions, using X-ray absorption fine structure (XAFS). XAFS is an oscillatory structure in the X-ray absorption spectrum above the absorption edge of the constituent atoms (Koningsberger & Prins, 1988). XAFS is a result of the photoelectron scattering by the surrounding atoms and it provides local structural information around the X-ray excited atom of interest. Analysis of the XAFS traditionally breaks up into two parts: XANES (X-ray absorption near-edge structure) and EXAFS (extended X-ray absorption fine structure). XANES refers to the region close to the edge (within about 30 eV) and is sensitive to the oxidation state of the excited atom. EXAFS, on the other hand, refers to the oscillations well above the edge ($\geq$30 eV) and gives local structural information about the excited atom. XAFS, being element specific, can extract detailed structural changes around the individual atomic species (Heald & Tranquada, 1989). For example, XAFS at the Ni *K*-edge can (in principle) detect possible Ni–Pt alloy formation (Nash & Singleton, 1989; Okamoto, 2010) at the Ni–Pt interface, or Ni–C compound formation (Singleton, 1989; Merschrod *et al.*, 1998) at the Ni–C interface. These changes are typically reflected in coordination or bond lengths in EXAFS results or white-line features (oxidation state) in XANES.

The layers and interfaces of the ML can be selectively filtered for information by the X-ray standing-wave (XSW) technique. A standing-wave field is generated within the periodic multilayer as a result of a superposition of incident and diffracted waves when X-rays are Bragg reflected by the periodic multilayer (Ghose & Dev, 2001; Bera *et al.*, 2007*a*). The equi-intensity planes of the standing-wave field are parallel to and have the periodicity of the diffracting planes in the periodic multilayers. At an angle of incidence corresponding to the rising edge of the diffraction peak, the antinodal planes of the standing-wave field lie between the diffracting planes. As the angle of incidence increases, the antinodal planes move continuously inward onto the diffracting planes at the falling edge of the diffraction peak. Over the angular region of the Bragg reflection, the emission of fluorescent X-rays (Ghose & Dev, 2001; Bera *et al.*, 2007*a*) from the periodic multilayer is strongly modulated, being at a maximum (minimum) when the antinodal (nodal) planes coincide with positions of the atoms in the periodic multilayer. Bragg diffraction is also obtained from a multilayer with a slightly varying period and consequently an XSW is generated in such graded MLs. By scanning across the Bragg angle we center the antinode successively in each layer. The present system is the same as that described by Roy & Dev (2011) and Roy *et al.* (2012). On the Bragg peak (Fig. 1*a*) we select two angles on the rising ($\theta = 0.554^\circ$) and falling ($\theta = 0.638^\circ$) edges of the Bragg peak which we refer to as 'low' and 'high', respectively, in this manuscript. For the present pristine ML system, although the low angle corresponds to the location of antinodes on the C layer, rising edges of the antinodes coincide with the Ni/C interfaces (Fig. 1*b*). Fluorescence-mode Ni *K*-edge XAFS for this angle, therefore, yields the structural information around Ni diffused into the C layer. At the high angle, the antinodes coincide with C/Pt interfaces (Fig. 1*b*). However, the main contribution to Ni fluorescence comes from the relatively denser Ni atomic concentration at the Pt/Ni interfaces as the falling edges of the antinodes coincide

with these interfaces (Fig. 1*b*). Therefore, Ni *K*-edge XAFS at high angle reveals the Ni environment predominantly at the Pt/Ni interface.[1] Any dissolved Ni, although expected to be in very small amounts at this interface, can contribute to the observed Ni fluorescence. In the irradiated ML, the XSW pattern shifts owing to changes in structure (mixing) and density. At low angle, the antinodes of the XSW coincide with the C layer of the irradiated ML while the nodes coincide with the Ni/Pt interface [or, rather, at the middle of the mixed Ni–Pt layer (Roy *et al.*, 2012) (black curve, Fig. 1*c*). Ni *K*-edge XAFS at this angle, for the irradiated ML, reveals structural information around Ni diffused into the C layer (as in the pristine ML). At high angle, the antinodes of the XSW shift to the Ni/Pt interface or the middle of the Ni–Pt layer (instead of the C/Pt interface as in the pristine ML) while the nodes are located in the C layer (blue curve, Fig. 1*c*). Therefore, Ni *K*-edge XAFS at this angle reveals the structural information around Ni at the Ni/Pt interface of the irradiated ML.

The structural model is retrieved mainly from the XAFS coordination results. We theoretically calculated the coordination number for various degrees of interfacial mixing and compared with the XAFS results. The theoretical coordination calculation is non-trivial, having to include the variation in field intensity over the individual layers of the ML from the XSW pattern (since this causes variation in the number of Ni atoms excited at different depths over a period of the ML sample).[2] With rigorous XAFS analysis we are able to derive finer (beyond XRR/XRF/XTEM) microstructural details, *e.g.* quantification of intermixing, chemical nature of mixing, cluster identification. The most important outcome is the identification of bimetallic nanoclusters formed within the irradiated C matrix.

2. Experimental details

A Pt/Ni/C multilayer constituting N = 15 tri-layers and tri-layer periodicity $d \simeq 7$ nm was deposited on a float glass substrate by the ion beam sputtering technique (Roy *et al.*, 2007). 2 MeV Au^{2+} ions were used for irradiation of the ML sample. EXAFS measurements were carried out on the pristine and one irradiated sample. X-ray reflectivity (XRR) and XSW experiments were carried out on several irradiated samples (Roy *et al.*, 2012). However, for EXAFS experiments the sample irradiated at the highest fluence (2×10^{15} ions cm^{-2}) was chosen. XAFS data were collected in the fluorescence mode at the Ni *K*-edge (8.333 keV) at the ROEMO (E2) beamline at Hamburg Synchrotron Radiation Laboratory (HASYLAB) at DESY, Germany. A pair of Si (111) crystals in parallel geometry was used as a monochromator to filter out the wavelengths. The first Si (111) crystal in the path of the incident beam was given suitable offset (from parallel geometry) to suppress higher harmonics from the monochromator. During an energy scan of the EXAFS experiments an appropriate adjustment of the angle of incidence was made in order to keep the antinodal positions

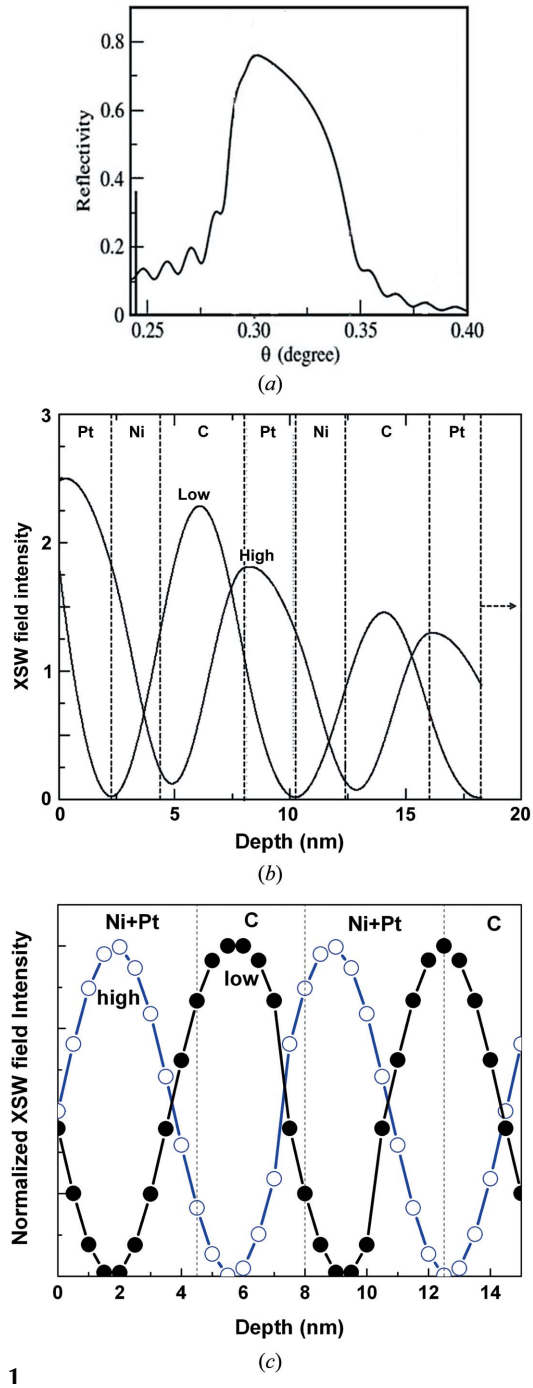

Figure 1
(*a*) First-order Bragg peak. The positions of the antinodes and nodes of the XSW formed within the first few layers (seven consecutive layers from the surface) of our graded Pt/Ni/C multi-trilayer are shown in (*b*) for the pristine ML and in (*c*) for the irradiated ML. The black curve corresponds to the angle chosen on the left-hand (lower angle) side of the Bragg peak while the blue curve corresponds to the angle chosen at the right-hand (high angle) side of the Bragg peak.

[1] In the system under consideration, the thicknesses of the Pt layer and Ni layer are 23 Å and 22 Å, respectively. The thickness of the C layer was varied from 29.7 Å (at the bottom-most layer) to 35.7 Å (at the top-most layer), since the system is a depth-graded multilayer. Despite the location of antinodes at the interfaces, there will be some contribution to the signal from the non-interfacial regions of the layers.

[2] With the penetration depth of 2 MeV Au^{2+} ions being of the order of micrometers, ions pass through the ML sample and become embedded deep in the substrate; the variation owing to the ion impact factor is negligible.

within the sample unchanged. A Si (Li) detector was used to collect the fluorescence photons. The data were processed using *ATHENA* software and the background parameters were chosen so that the data suffer from least artefacts owing to processing. The extracted XAFS oscillations, $\chi(k)$, were Fourier-transformed into real space for fitting $\{k = [2m(E - E_0)/\hbar^2]^{1/2}$, where m is the electron mass and E_0 is the edge energy of the relevant absorption edge$\}$. An initial structural model was reasonably constructed, for which the theoretical scattering amplitudes and phase shifts were generated by *FEFF6.1*. The model parameters were allowed to vary while fitting (using *FEFFIT*) to yield the best-fit values for bond lengths (r), coordination numbers (N) and Debye–Waller factors (σ^2). The R factor was considered as an estimate of the quality of fit (Newville, 2001; Newville *et al.*, 1995).

Table 1
XAFS fit results.

Bond	ML	N	σ^2 (Å^2)	R (Å)	Theoretical R (Å)
Low angle					
Ni–Ni	Pristine	5.46 ± 0.12	0.018 ± 0.0004	2.445 ± 0.003	2.48
	Irradiated	6.24 ± 0.17	0.021 ± 0.0005	2.612 ± 0.001	
Ni–C	Pristine	0.88 ± 0.18	0.016 ± 0.006	1.964 ± 0.007	2.00
	Irradiated	0.33 ± 0.18	0.016 ± 0.006	1.964 ± 0.007	
Ni–Pt	Pristine	–	–	–	2.60
	Irradiated	4.14 ± 0.14	0.024 ± 0.002	2.727 ± 0.007	
High angle					
Ni–Ni	Pristine	7.27 ± 1.11	0.021 ± 0.003	2.54 ± 0.01	2.48
	Irradiated	8.49 ± 0.92	0.025 ± 0.003	2.60 ± 0.01	
Ni–Pt	Pristine	3.4 ± 1.04	0.016 ± 0.009	2.72 ± 0.04	2.60
	Irradiated	3.51 ± 0.92	0.02 ± 0.01	2.76 ± 0.03	

3. Results and discussion

The XAFS data sets were analyzed for the first coordination shell around Ni. The rather large noise (possibly owing to a disordered interface) in the data precluded higher shell analysis. However, the first-shell (nearest-neighbor) analysis is found to sufficiently extract the irradiation-induced structural changes (shown below). The correlation-free coordination (N) and Debye–Waller factor were obtained by simultaneously fitting each dataset for k^w (w = 1, 2) (simultaneous fitting of the datasets was necessary in order to have sufficient variables for fitting). The data were fit over k-range 2.2–8 Å^{-1} and r-range 1.2–3.4 Å. The results are listed in Table 1. An example of fit quality (R factor = 0.001–0.014) is shown in Fig. 2(b). Several fitting strategies were considered to test the robustness of the fit parameters, such as (or non-) inclusion of a third cumulant (the third cumulant is a measure of the anharmonicity in the atomic distribution) into disorder, (or non-) constraining the coordination number around Ni to 12 (f.c.c.) or that between the pristine and irradiated MLs to be the same. The error bars in Table 1 reflect the maximum possible variation from all these fits.

3.1. Low angle (C layer and its interfaces with Ni and Pt)

XAFS data for the pristine ML at low angle was fit by considering Ni–Ni and Ni–C scattering paths (any attempt to include Ni–Pt path resulted in a poor fit; this is not surprising as there are nodes at the Pt/Ni interfaces). The large error bars for $N_{\mathrm{Ni–C}}$ are due to the extremely low Ni–C coordination.

From Fig. 1(b) it is clear that in the data there are contributions from parts of the Ni layer, Ni/C interface and (possible) diffused Ni atoms in the bulk C layer. Considering interfacial planes to be {111}/{100}/{110} and taking into account the relative variation in field intensity across the ML (as explained earlier) (refer to Fig. 1a), the weighted-average

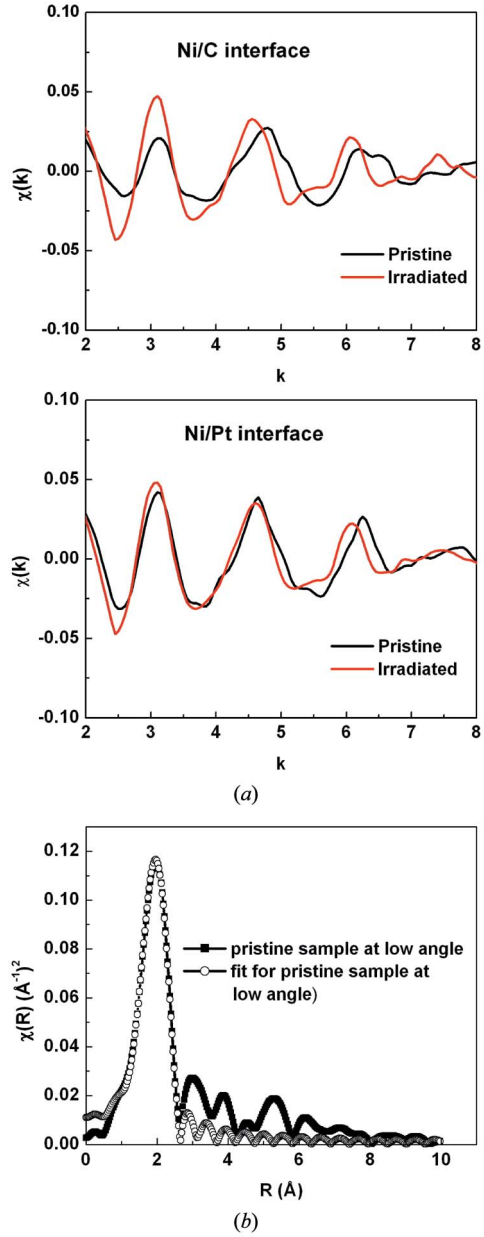

Figure 2
(a) Comparison of data in k-space before and after irradiation for the Ni/C interface (top) and the Ni/Pt interface (bottom). (b) Comparison of data with fit.

Ni–Ni coordination may be formulated as (Swaminathan *et al.*, 2004; Robinson, 1986; Fukunaga *et al.*, 2001)

$$N_{\mathrm{Ni-Ni}} = \frac{\left[\left(12\,\frac{\int I_{\mathrm{Ni}}}{\int I_0}\,N_A\right) + \left(8.33\,\frac{\int I_{\mathrm{Ni/C}}}{\int I_0}\,N_B\right)\right]}{\left(\frac{\int I_{\mathrm{Ni}}}{\int I_0}\,N_A\right) + \left(\frac{\int I_{\mathrm{Ni/C}}}{\int I_0}\,N_B\right)}, \qquad (1)$$

where N_A is the number of Ni atoms in the Ni layer, N_B is the number of interfacial Ni atoms, I_{Ni} is the intensity in the Ni layer, I_{C} is the intensity in the C layer, $I_{\mathrm{Ni/C}}$ is the intensity at the Ni/C interface, I_0 is the maximum intensity, in this case I_{C}.[3][4][5]

The first and second terms in the numerator reflect the contribution from Ni—Ni bonds in the Ni layer and at the Ni/C interface. (Note that Ni cluster formation inside the C layer is excluded preliminarily.) The denominator represents the sum of Ni atoms excited in the Ni layer and Ni/C interface. Assuming the interfacial roughness ($\sigma_{\mathrm{Ni-C}}$ = 1.7 Å, from reflectivity experiments) to be preliminarily representative of the interfacial extent, and the thickness of the Ni layer = 22 Å, the interface volume ratio $N_B/(N_A + N_B) = 7\%$. However, this ratio should have yielded $N_{\mathrm{Ni-Ni}}$ = 11.63 from equation (1) (instead of 5.4 in Table 1).

On the other hand, the average interfacial Ni–C coordination (for adsorption) may be formulated as

$$(N_{\mathrm{Ni-C}})_{\max} = \frac{3.67\,\frac{\int I_{\mathrm{Ni/C}}}{\int I_0}\,N_B}{\left(\frac{\int I_{\mathrm{Ni}}}{\int I_0}\,N_A\right) + \left(\frac{\int I_{\mathrm{Ni/C}}}{\int I_0}\,N_B\right)}. \qquad (2)$$

From this equation $N_{\mathrm{Ni-C}}$ = 0.37 (instead of 0.879 in Table 1). A lower $N_{\mathrm{Ni-Ni}}$ (in Table 1) and higher $N_{\mathrm{Ni-C}}$ (compared with calculated results from the above equation) suggests replacement of some Ni near neighbors by C atoms, possibly owing to additional (random) diffusion of Ni into the C layer (beyond the reflectivity-derived simplistic binary model of layer plus interface) (Fig. 3). Solving (2) for XAFS-derived coordination yielded this additional Ni proportion to be 26%.[6] Thus, the salient conclusion on the pristine Ni/C interfacial structure, from XAFS (and beyond XRR), is the existence of a significant proportion of sporadic pre-diffused Ni atoms within the C layer. The implications of this finding will be evident later in this paper.

[3] Bulk Ni f.c.c. lattice has 12 neighbors while interfacial Ni has nine neighbors. Three missing neighbors correspond to dangling bonds for the {111} plane. In the case of the {110} and {100} planes, interfacial Ni has eight neighbors and the four missing neighbors correspond to dangling bonds. Since the layers are polycrystalline in the sample, we have to consider an average over these three planes.

[4] The intensity variation (Fig. 1) in the various layers is normalized with respect to the intensity in (i) the C layer for low angle of the Bragg peak and (ii) the Pt layer for high angle of the Bragg peak.

[5] There are no Ni atoms at the C/Pt interface.

[6] Total $N_{\mathrm{Ni-C}}$ = 0.88, out of which 0.37 is interfacial. This implies that 0.51 is in the C layer. Now, each Ni atom in the C layer has two C coordination (amorphous carbon). 2 × (total number of Ni atoms) contribute to $N_{\mathrm{Ni-C}}$ = 0.51. Therefore the percentage of Ni atoms diffused into the C layer = 0.51/2 = 26%.

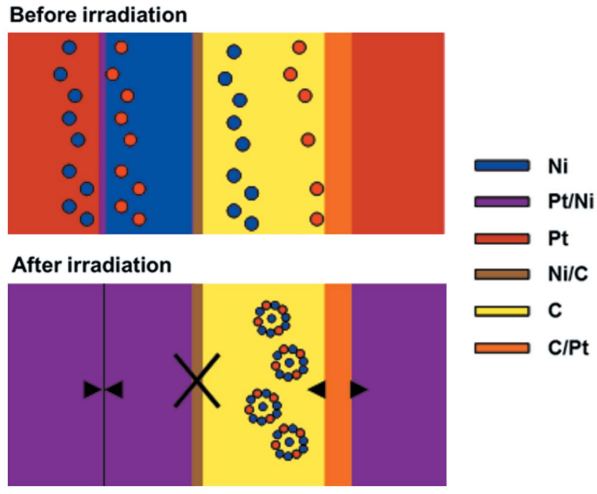

Figure 3
Structural model for the ML before (top) and after (bottom) irradiation.

The nature of the Ni—C bond is determined to be chemical from XANES: XANES at the Ni *K*-edge (Fig. 4*a*), for the pristine ML, shows conspicuous (positive) deviation of the Ni valence from that of pure Ni (*i.e.* zero oxidation state). We attribute the integrity of the Ni/C interface, during irradiation, to this chemical binding.

The data for the irradiated ML were best fit by the Ni–C, Ni–Ni and Ni–Pt scattering paths [simulations for different

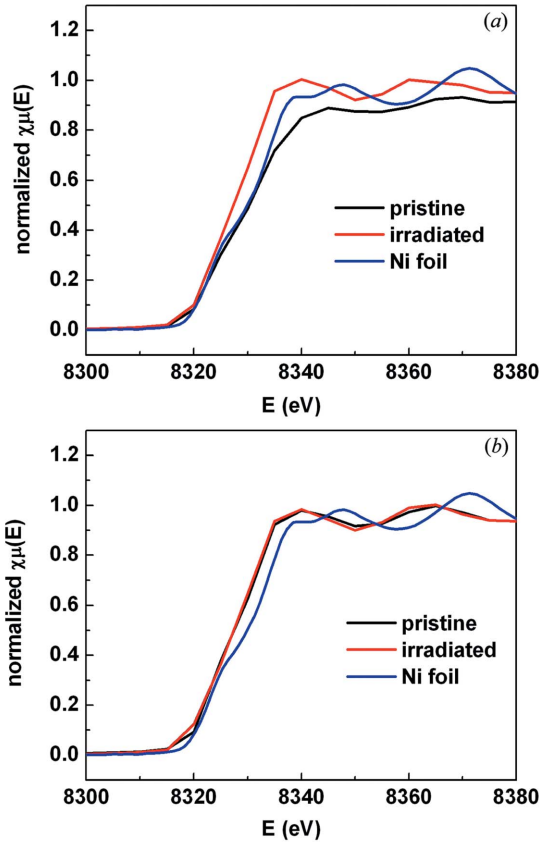

Figure 4
XANES at (*a*) the Ni/C interface and (*b*) the Ni/Pt interface.

values of N_{Ni-Ni} (and N_{Ni-Pt}) reveal a resolution limit of $\Delta N = 2$]. The emergence of the Ni–Pt coordination (in contrast to the pristine ML) is consistent with XTEM results and is due to irradiation-induced diffusion of Pt atoms into the C layer (suggested by XRR). [Pt/C interfaces (Bera *et al.*, 2003; Lodha *et al.*, 1994; Evans & Kent, 1987) are reported to be vulnerable owing to the absence of the Pt—C chemical bond (Albe *et al.*, 2002), unlike Ni—C (Struis *et al.*, 2009). This is consistent with the increase in roughness with irradiation reported by Roy *et al.* (2012): $\sigma_{Pt/C}$ increases by ~400% while the corresponding increase in $\sigma_{Ni/C}$ is by 32%.] The bond-length changes are consistent with the mixing of Ni and Pt. The Ni—Ni bond length (2.44 Å), which is close to the metallic value (2.48 Å) before irradiation, expands (to 2.6 Å) towards the Pt—Pt bond length (2.7 Å) after irradiation. This bond-length change is duly directed towards accommodating the larger intercalated Pt atoms.

While XTEM indicates the formation of Pt–Ni nanoclusters, it is unable to determine their exact configuration. We consider various models of nanoclusters to deduce the configuration of Ni–Pt within the C layer: (i) isolated clusters of Ni and Pt; (ii) Ni core–Pt shell; (iii) Pt core–Ni shell; (iv) Ni-centered icosahedral bimetallic cluster [the icosahedral model has been considered since this is a highly disordered system; in highly disordered systems (for example, metallic glass), such icosahedral structural units have been observed (Greer, 1993)] and (v) Pt-centered icosahedral bimetallic cluster.

For this, the contributions to N_{Ni-Ni} from the Ni/C interface, Ni + Pt mixed layer and within the C layer were decoupled.[7] Subtracting the interfacial contribution and Ni + Pt layer contribution from the total in Table 1, N_{Ni-Ni} (from the C layer) and N_{Ni-Pt} are calculated to be 6.35 and 3.64, respectively. Next, for models (i)–(iv) we calculated N_{Ni-Ni} and N_{Ni-Pt} for different surface-volume ratios of the number of Ni atoms[8] (*i.e.* different cluster sizes of Ni).

Model (i) is ruled out since the experimentally deduced N_{Ni-Ni} (~6.35) is significantly lower than that for the smallest Ni cluster. On the other hand, significant N_{Ni-Pt} (~3.64) rules out isolated Pt clusters. The same logistics rule out model (ii), since the latter would have resulted in a minimum N_{Ni-Ni} of ~9. Model (iii) is ruled out since our $N_{Ni-Pt} > 0.3$.[9] Models (iv)–(v) would have resulted in $N_{Ni-Ni} + N_{Ni-Pt} \simeq 7$. The same being ~9 from our XAFS results rules out 13-atom icosahedral clusters.

Therefore, Ni-centered Ni–Pt bimetallic clusters, having Ni:Pt = 0.6:0.4, highly disordered beyond the first shell, may be the best representation for the Ni/Pt configuration within the C layer. The first-shell radius of the clusters is estimated to be ~0.25 nm, corresponding to the Ni–Pt bond length in Table 1. The solution is consistent with Ni–Pt alloy formation, as indicated by the Ni–Pt binary phase diagram for this atomic concentration ratio. Previous reports on Ni/Pt alloys have shown clusters of this particular composition to be ferromagnetic (Kumar *et al.*, 2005, 2006; Cadeville *et al.*, 1986). In this context the role of the chemical/physical nature of the interfaces may be emphasized. It determines the relative ratio of metallic diffusion into the C matrix, which eventually determines the composition or density of the bimetallic clusters. With physical interfaces (Pt/C, in this case) being more susceptible to ion irradiation than chemical interfaces (*e.g.* Ni/C), a large number of Pt atoms diffuse into the C layer (on irradiation) from the Pt/C interface as compared with Ni atoms from the Ni/C interface. (Note that, from our XAFS coordination results, the Ni/C interface is unaffected by ion irradiation.)

A remarkable aspect of these clusters is the presence of large disorder beyond the nearest neighbor, similar to our observation for multi-component metallic glasses. Notably, ordering features persisted up to the second nearest neighbor for our bimetallic glasses. The striking difference in the degree of disorder between multi-component and bimetallic glasses is understandably consistent with the 'confusion principle' (Greer, 1993). In contrast, we observe that the bimetallic clusters formed on the C matrix (induced by ion irradiation) are far more disordered and resemble multi-component cluster characteristics. The carbon matrix possibly helps the amorphous structure (Wang *et al.*, 1997). Highly disordered clusters, resembling a glassy structure, find use as patterned magnetic recording media. Their amorphous nature promotes growth in the preferred orientation (Wang *et al.*, 2012). Moreover, with glasses being defect-free, the issue of different parts having different switching fields owing to defects can be avoided (during writing) (Xu *et al.*, 2004). Thus, ion irradiated Pt/Ni/C ML offers promise as a magnetic device.

The subsequent design goal in the ion-irradiation-based fabrication method should be the optimization of the cluster composition [to tune T_c, susceptibility *etc.* (Kumar *et al.*, 2005)], size and inter-cluster separation (to tune luminescence properties) by selection of matrix and metals, controlling interfacial charge transfer, layer thickness, ion flux, *etc*. The question arises as to whether these bimetallic clusters would affect the functionality of the mirror. Since plasmon absorption is always in the visible range, the reflectivity of the mirror remains unaffected.

3.2. High angle (Ni–Pt interface)

The data for both the pristine and the irradiated MLs were best fit by Ni–Ni and Ni–Pt scattering paths. (Note that any attempt to include the Ni–C path resulted in a bad fit.) Fourier transformed data for both the MLs are shown in Fig. 5. Metallic interfaces are generally marked by intermixing (Holmström *et al.*, 2004) between the layers: Ni–Pt forms alloys (Choi *et al.*, 1985; Bommannavar *et al.*, 1985) at very low energies. Lower N_{Ni-Ni} (~7.3) and increased N_{Ni-Pt} (~3.4), for the pristine ML, compared with those theoretically calculated [replacing I_C by I_{Pt} (intensity in the Pt layer) and $I_{Ni/C}$ by $I_{Ni/Pt}$

[7] The integrated intensities for each interface and layer were calculated. The total N_{Ni-Ni} has contributions from the Ni + Pt mixed layer plus the C layer plus the Ni/C interface: $[N_{Ni-Ni}]_{Total} = (N_{C\,layer} \int I_C + N_{Ni+Pt\,mixed\,layer} \int I_{Ni+Pt} + N_{Ni/C} \int I_{Ni/C}) / (\int I_C + \int I_{Ni+Pt} + \int I_{Ni/C})$.

[8] $N_{Ni-Ni} = 12(1 - x) + 9x$; $N_{Ni-Pt} = 3x$.

[9] A Pt-core Ni-shell would imply that surface Pt atoms see an average of three Ni nearest neighbors, assuming the surface to be (111); so each Ni atom will see 1/3 = 0.3 Pt atoms.

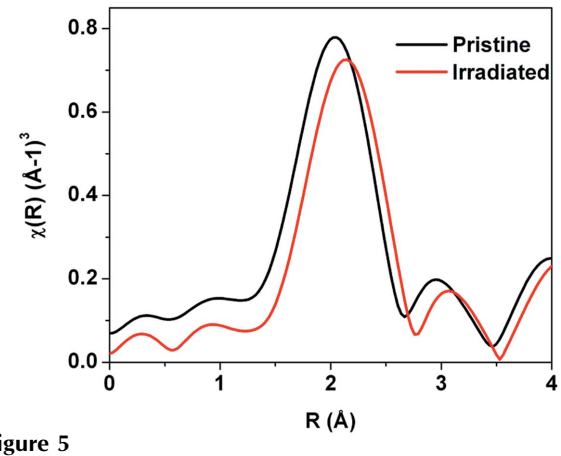

Figure 5
Fourier transform for both MLs at the Ni/Pt interface.

(intensity at the Ni/Pt interface) in equations (1) and (2)] for an ideal sharp interface[10] implies pre-existing intermixing, consistent with XRR. From the coordination ratio $N_{\mathrm{Ni-Ni}}$:$N_{\mathrm{Ni-Pt}}$ (and density), the atomic concentration ratio Ni:Pt was calculated to be 0.82:0.16. The Ni–Pt binary phase diagram suggests the possibility of alloy formation for this concentration ratio (Singleton, 1989). This is further supported by XANES at the Ni *K*-edge (Fig. 4*b*) for the pristine ML, which shows conspicuous (negative) deviation from that of pure Ni (*i.e.* zero oxidation state). It implies charge transfer to Ni at this interface, most likely from Pt (Shevchik & Bloch, 1977). Therefore, the Ni–Pt alloy could be a reasonably justified structural representation for this interface.

For the irradiated ML, $N_{\mathrm{Ni-Ni}}$ and $N_{\mathrm{Ni-Pt}}$ were calculated for various degrees of interfacial mixing and by including the intensity variation. It is deduced that interlayer diffusion of 54% Pt → Ni and 22% Ni → Pt best matches with the XAFS coordination.[11] The asymmetry in diffusion is consistent with a pre-existing vacancy in the Ni layer (owing to 26% Ni → C diffusion), which accommodates the apparently extra Pt atoms.[12]

Comparing the results for the pristine and irradiated Ni/Pt interfaces, we observe significant enhancement in interfacial broadening (consistent with XRR) owing to ion-driven diffusion, depicted in Fig. 3. The oxidation state of Ni remains unchanged, as confirmed by the similarity in the XANES spectra (Fig. 4*b*) for both the pristine and irradiated MLs. Thus, the XAFS conclusion of the Ni/Pt interface (beyond XRR) is the quantification of the degree of atomic mixing and the alloy composition of the interface.

[10] An ideal sharp interface implies that there is no diffusion between the layers beyond the interface.

[11] The following equations were used to deduce the degree of mixing between the Ni and Pt layers: $N_{\mathrm{Ni-Ni}} = [12(N_A - \Delta N)\int I_{\mathrm{Ni}}/\int I_0 + (8.33\int I_{\mathrm{Ni/Pt}}/\int I_0)N_B]/[(\int I_{\mathrm{Ni}}/\int I_0)N_A + (\int I_{\mathrm{Ni/Pt}}/\int I_0)N_B]$, $N_{\mathrm{Ni-Pt}} = [12\Delta N\int I_{\mathrm{Pt}}/\int I_0 + (1/12)\Delta N\int I_{\mathrm{Ni}}/\int I_0 + 3.67(\int I_{\mathrm{Ni/Pt}}/\int I_0)N_B]/[(\int I_{\mathrm{Pt}}/\int I_0)\Delta N + (\int I_{\mathrm{Ni}}/\int I_0)N_A + (\int I_{\mathrm{Ni/Pt}}/\int I_0)N_B]$, where ΔN is the number of Ni atoms exchanged, N_A is the number of Ni atoms in the Ni layer, N_B is the number of Ni atoms at the Ni/Pt interface.

[12] Note that the total Ni vacancy, owing to diffusion, = 26% (Ni → C) + 22% (Ni → Pt) = 48%, is consistent with the total Pt → Ni diffusion = 54%.

4. Conclusion

We have probed the structural changes of a Pt/Ni/C multi trilayer upon ion irradiation, using a combination of XSW and Ni *K*-edge XAFS. Our XAFS (and XANES) analysis detects pre-existing charge and atomic transfer at pristine Ni/C and Ni/Pt interfaces (directly) and determines the character of Pt/C to be physically adsorbed Pt–C (indirectly). Metallic diffusion into the C matrix is observed to be directly correlated with the extent of charge transfer at the metal/C interface. Physical adsorption (at the Pt/C interface) evidently encourages interfacial diffusion (Pt into C). Following irradiation, Pt atoms from the disrupted Pt/C interfaces migrate towards pre-diffused Ni atoms within the C layer to form Ni-centered Ni–Pt bimetallic nanoclusters. These clusters, having Ni:Pt = 60:40, are ferromagnetic in nature. The clusters are highly disordered beyond the nearest neighbor and resemble the short-range order of multi-component glasses. Such disordered clusters on the C matrix have promising applications as magnetic devices.

References

Albe, K., Nordlund, K. & Averback, R. S. (2002). *Phy. Rev. B*, **65**, 195124.
Bera, S., Bhattacharjee, K., Kuri, G. & Dev, B. N. (2007*a*). *Phys. Rev. Lett.* **98**, 196103.
Bera, S., Goswami, D. K., Bhattacharjee, K., Dev, B. N., Kuri, G., Nomoto, K. & Yamashita, K. (2003). *Nucl. Instrum. Methods Phys. Res. B*, **212**, 530–534.
Bera, S., Roy, S., Bhattacharjee, K., Kuri, G. & Dev, B. N. (2007*b*). *J. Appl. Phys.* **102**, 014308.
Bera, S., Satpati, B., Goswami, D. K., Bhattacharjee, K., Satyam, P. V. & Dev, B. N. (2006). *J. Appl. Phys.* **99**, 074301.
Bommannavar, A. S., Montano, P. A. & Yacaman, M. J. (1985). *Surf. Sci.* **156**, 426–435.
Cadeville, M., Dahmani, C. E. & Kern, F. (1986). *J. Magn. Magn. Mater.* **54–57**, 1055–1056.
Chakraborty, P. (1991). *Intl J. Mod. Phys. B*, **5**, 2133–2228.
Che, G., Lakshmi, B. B., Martin, C. R. & Fischer, E. R. (1999). *Langmuir*, **15**, 750–758.
Choi, M., Pease, D. M., Hines, W. A., Hayes, G. H., Budnick, J. I., Heald, S. M., Hasegawa, R. & Schone, H. E. (1985). *Phys. Rev. B*, **32**, 7670–7675.
Chopra, N., Wu, Y. & Kazmaeir, P. M. (2009). US Patent Application US 2009/0274834 A1.
Deivaraj, T. C., Chen, W. & Lee, J. Y. (2003). *J. Mater. Chem.* **13**, 2555–2560.
Dev, B. N. (2003). *Physics at Surfaces and Interfaces*, p. 121. Singapore: World Scientific.
Dev, B. N., Bera, S., Satpati, B., Goswami, D. K., Bhattacharjee, K., Satyam, P. V., Yamashita, K., Liedke, O. M., Potzger, K., Fassbender, J., Eichhorn, F. & Groetzschel, R. (2006). *Microelectron. Eng.* **83**, 1721–1725.
Evans, B. L. & Kent, B. J. (1987). *Appl. Opt.* **26**, 4491–4497.
Falcao, C. M. & Schuller, I. K. (1985). *Synthetic Modulated Structural Materials*. New York: Academic.
Fukunaga, T., Itoha, K., Orimo, S., Aoki, M. & Fujii, H. (2001). *J. Alloys Compd.* **327**, 224–229.
Ghose, S. K. & Dev, B. N. (2001). *Phys. Rev. B*, **63**, 245409.
Ghose, S. K., Goswami, D. K., Rout, B., Dev, B. N., Kuri, G. & Materlik, G. (2001). *Appl. Phys. Lett.* **79**, 467.
Greer, A. L. (1993). *Nature (London)*, **366**, 303–304.
Heald, S. M. & Tranquada, J. M. (1989). *J. Appl. Phys.* **65**, 290–293.

Holmström, E., Nordström, L., Bergqvist, L., Skubic, B., Hjörvarsson, B., Abrikosov, I. A., Svedlindh, P. & Eriksson, O. (2004). *Proc. Natl Acad. Sci. USA*, **101**, 4742–4745.
Jiang, H., Yao, X., Che, J., Wang, M. & Kang, F. (2004). *Ceram. Intl*, **30**, 1685–1689.
Kapta, K., Csik, A., Daroczi, L., Papp, Z., Beke, D. L., Langer, G. A., Greer, A. L., Barber, Z. H. & Kis-Varga, M. (2004). *Vacuum*, **72**, 85–89.
Koningsberger, D. C. & Prins, R. (1988). *X-ray Absorption: Principles, Applications and Techniques of EXAFS, SEXAFS and XANES*. New York: Wiley.
Kumar, U., Mukhopadhyay, P. K., Sanyal, B., Eriksson, O., Nordblad, P., Paudyal, D., Tarafder, K. & Mookerjee, A. (2006). *Phys. Rev. B*, **74**, 064401.
Kumar, U., Padmalekha, K. G., Mukhopadhyay, P. K., Paudyal, D. & Mookerjee, A. (2005). *J. Magn. Magn. Mater.* **292**, 234–240.
Lahiri, D., Chattopadhyay, S., Bunker, B. A., Doudna, C. M., Bertino, M. F., Blum, F., Tokuhiro, A. & Terry, J. (2005). *Phys. Scr.* T**115**, 776–780.
Li, W. & Haldar, P. (2010). *Electrochem. Solid State Lett.* **13**, B47–B49.
Lodha, G. S., Yamashita, K., Suzuki, T., Hatsukade, I., Tamura, K., Ishigami, T., Takahama, S. & Namba, Y. (1994). *Appl. Opt.* **33**, 5869–5874.
McWhan, D. B. (1985). *Synthetic Modulated Structure*, edited by L. L. Chang and B. C. Geisser, ch. 2, p. 43. New York: Academic Press.
Merschrod, E. M., Tang, S. H. & Hoffmann, R. (1998). *Z. Naturforsch. Teil B*, **53**, 322–332.
Nakajima, K., Aoki, S., Sudo, S. & Fujiwara, S. (1992). *Jpn. J. Appl. Phys.* **31**, 2864–2868.
Nash, P. & Singleton, M. F. (1989). *Bull. Alloy Phase Diagr.* **10**, 258–262.
Newville, M. (2001). *J. Synchrotron Rad.* **8**, 96–100.
Newville, M., Ravel, B., Haskel, D., Rehr, J. J., Stern, E. A. & Yacobi, Y. (1995). *Physica B*, **208**–**209**, 154–156.
Nicewarner-Peña, S. R., Freeman, R. G., Reiss, B. D., He, L., Peña, D. J., Walton, I. D., Cromer, R., Keating, C. D. & Natan, M. J. (2001). *Science*, **294**, 137–141.
Nose, K., Omata, T., Otsuka, S. & Matsuo, Y. (2009). *J. Phys. Chem C*, **113**, 3455–3460.
Okamoto, H. (2010). *J. Phase Equilib. Diffus.* **31**, 322.
Patton, S. T., Slocik, J. M., Campbell, Hu, J., Naik, R. R. & Voevodin, A. A. (2008). *Nanotechnology*, **19**, 405705.
Prabhuram, J., Zhao, T. S., Wong, C. W. & Guo, J. W. (2004). *J. Power Sources*, **134**, 1–6.
Qin, J., Shao, J. & Zhengxiu Fan, K. Y. (2007). *Chin. Opt. Lett.* **5**, 301–303.
Robinson, I. K. (1986). *Phys. Rev. B*, **33**, 3830–3836.
Roy, S., Bera, S. & Dev, B. N. (2007). *J. Nanosci. Nanotechnol.* **7**, 2182–2185.
Roy, S. & Dev, B. N. (2011). *Appl. Surf. Sci.* **257**, 7566–7572.
Roy, S., Ghatak, J. & Dev, B. N. (2012). *Appl. Surf. Sci.* **258**, 3967–3974.
Sella, C., Youn, K., Barchewitz, R., Arbaoui, M. & Krishnan, R. (1998). *Thin Solid Films*, **164**, 405–409.
Shevchik, N. J. & Bloch, D. (1977). *J. Phys. F*, **7**, 543–550.
Singleton, M. & Nash, P. (1989). *Bull. Alloy Phase Diagr.* **10**, 121–126.
Stearns, M. B. (1984). *J. Appl. Phys.* **55**, 1729.
Struis, R. P. W. J., Bachelin, D., Ludwig, C. & Wokaun, A. (2009). *J. Phys. Chem. C*, **113**, 2443–2451.
Swaminathan, R., McHenry, M. E., Sorescu, M., Diamandescu, L. & Calvin, S. (2004). *Proceedings of the Ninth International Conference on Ferrites (ICF-9)*, San Francisco, California, USA, p. 847.
Takacs, P. Z., Melendez, J. & Colbert, J. (1985). *International Conference on X-ray and VUV Synchrotron Radiation Instrumentation*, 29 July–2 August 1985, Stanford University, California. USA.
Toshima, N. & Yonezawa, T. (1998). *New J. Chem.* **22**, 1179–1201.
Toulemonde, M., Dufour, C. & Paumier, E. (1992). *Phys. Rev. B*, **46**, 14362–14369.
Wang, G., Wu, H., Wexler, D., Liu, H. & Savadogo, O. (2010). *J. Alloys Compd.* **503**, L1–L4.
Wang, W.-H., Wei, Q. & Bai, H. Y. (1997). *Appl. Phys. Lett.* **71**, 58–60.
Wang, Y., Sharma, P. & Makino, A. (2012). *J. Phys. Condens. Matter*, **24**, 076004.
Wang, Z. G., Dufour, C., Paumier, E. & Toulemonde, M. (1994). *J. Phys. Condens. Matter*, **6**, 6733–6750.
Weller, D., Baglin, J. E. E., Kellock, A. J., Hannibal, K. A., Toney, M. F., Kusinski, G., Lang, S., Folks, L., Best, M. E. & Terris Jr, B. D. (2000). *Appl. Phys.* **87**, 5768–5770.
Wheat, P. M., Marine, N. A., Moran, J. L. & Posner, J. D. (2010). *Langmuir*, **26**, 13052–13055.
Wong, M. S., Alvarez, P. J. J., Fang, Y.-I., Akcin, N., Nutt, M. O., Miller, J. T. & Heck, K. N. (2008). *J. Chem. Technol. Biotechnol.* **84**, 158–166.
Xu, Y. F., Yan, M. L. & Sellmyer, D. J. (2004). *J. Nanosci. Nanotechnol.* **7**, 206–224.
Yamashita, K., Serlemitsos, P. J., Tueller, J., Barthelmy, S. D., Bartlett, L. M., Chan, K. W., Furuzawa, A., Gehrels, N., Haga, K., Kunieda, H., Kurczynski, P., Lodha, G., Nakajo, N., Nakamura, N., Namba, Y., Ogasaka, Y., Okajima, T., Palmer, D., Parsons, A., Soong, Y., Stahl, C. M., Takata, H., Tamura, K., Tawara, Y. & Teegarden, B. J. (1998). *Appl. Opt.* **37**, 8067–8073.
Zhang, W. M., Hu, J. S., Ding, H. T., Wan, L. J. & Song, W. G. (2009). *Anal. Chem.* **81**, 2815–2818.